Volume 14
Number 20
28 May 2022
Pages 7429-7758

Nanoscale

rsc.li/nanoscale

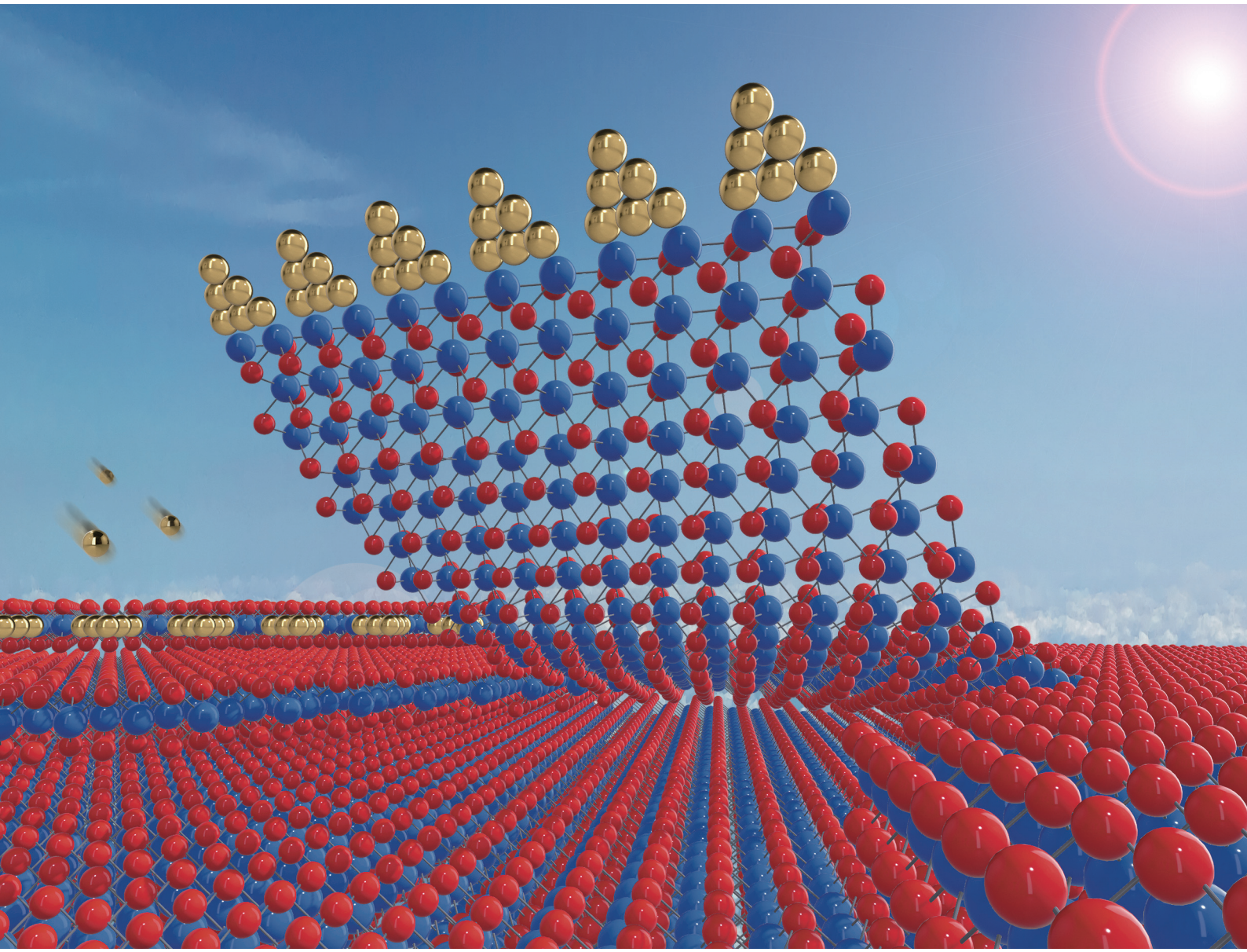

ISSN 2040-3372

ROYAL SOCIETY OF CHEMISTRY

PAPER
Xiuhua Xie, Xiaoli Sun, Jishan Liu, Dezhen Shen *et al.*
Directed exfoliating and ordered stacking of transition-metal-dichalcogenides

NCNST

Nanoscale

ROYAL SOCIETY OF CHEMISTRY

PAPER

View Article Online
View Journal | View Issue

Check for updates

Cite this: *Nanoscale*, 2022, **14**, 7484

Directed exfoliating and ordered stacking of transition-metal-dichalcogenides†

Yanshuang Li, [a,b] Xiuhua Xie, *[a] Binghui Li,[a] Xiaoli Sun,*[c] Yichen Yang,[d] Jishan Liu,*[d,e] Jiying Feng,[f] Ying Zhou,[f] Yuanzheng Li, [f] Weizhen Liu,[f] Shuangpeng Wang, [g] Wei Wang,[g] Huan Zeng,[a,b] Zhenzhong Zhang,[h] Dawei Shen[d] and Dezhen Shen*[a]

Received 22nd November 2021,
Accepted 2nd April 2022

DOI: 10.1039/d1nr07688d

rsc.li/nanoscale

Two-dimensional van der Waals crystals provide a limitless scope for designing novel combinations of physical properties by controlling the stacking order or twist angle of individual layers. Lattice orientation between stacked monolayers is significant not only for breaking the engineering symmetry but also for the study of many-body quantum phases and band topology. Thus far the state-of-the-art exfoliation approaches focus on the achievements of quality, size, yield, and scalability, while lacking sufficient information on lattice orientation. Consequently, interlayer alignment is usually determined by later experiments, such as the second harmonic generation spectroscopy, which increase the number of trials and errors for a designed artificial ordering and hampered the efficiency of systematic study. Herein, we report a lattice orientation distinguishable exfoliation method *via* gold favor epitaxy along the specific atomic step edges, meanwhile, fulfilling the requirements of high-quality, large-size, and high-yield monolayers. Hexagonal- and rhombohedral-stacking configurations of bilayer transition metal dichalcogenides are built directly at once as a result of foreseeing the lattice orientation. Optical spectroscopy, electron diffraction, and angle-resolved photoemission spectroscopy are used to study crystal quality, symmetric breaking, and band tuning, which support the exfoliating mechanism we proposed. This strategy shows the ability to facilitate the development of ordering stacking especially for multilayers assembling in the future.

Disassembling and reassembling two-dimensional (2D) materials into expected lattice configurations, give rise to intriguing quantum phases. As a consequence of stacking two layers of van der Waals (vdWs) materials, whether a lattice mismatch or twist angle existence, there is an additional periodicity as well as moiré superlattices,[1,2] which can alter the low-energy electronic structure and hence the particle correlations. Various correlated and topological phases were firstly observed in twisted bilayer graphene at the magic angle, such as unconventional superconductivity,[3] correlated insulators,[4] orbital Chern ferromagnets,[5] to name a few. As complementary to graphene-based moiré systems, transition metal dichalcogenides (TMDs), notably MoS_2, WS_2, $MoSe_2$, WSe_2, with homojunctions and heterojunctions, have more advantages for realizing model quantum Hamiltonians. For example, Hubbard model physics has been simulated in twist-TMDs, due to the simpler moiré band structure.[6–8] Generalized Wigner crystal has also been explored,[9–11] attributed to the moiré flat bands, which are generally considered to be formed in a larger range of twist-angles, tolerating the twist-angle disorder.[12] Moreover, benefiting from the strong matter–light interactions and deep tunable moiré potentials (100 to 200 meV),[13] bosonic quantum many-body effects are formed at higher temperatures.[14,15] TMDs-based moiré systems, actually, are robust quantum simulators for the study of strong correlations and band topology.[16–21]

[a]*State Key Laboratory of Luminescence and Applications, Changchun Institute of Optics, Fine Mechanics and Physics, Chinese Academy of Sciences, No. 3888 Dongnanhu Road, Changchun, 130033, People's Republic of China. E-mail: xiexh@ciomp.ac.cn, shendz@ciomp.ac.cn*
[b]*University of Chinese Academy of Sciences, Beijing 100049, People's Republic of China*
[c]*Institute of Theoretical Chemistry, Jilin University, Changchun 130023, People's Republic of China. E-mail: sunxiaoli@jlu.edu.cn*
[d]*Center for Excellence in Superconducting Electronics, State Key Laboratory of Functional Materials for Informatics, Shanghai Institute of Microsystem and Information Technology, Chinese Academy of Sciences, Shanghai 200050, China. E-mail: jishanliu@mail.sim.ac.cn*
[e]*Center of Materials Science and Optoelectronics Engineering, University of Chinese Academy of Sciences, Beijing 100049, China*
[f]*Key Laboratory of UV-Emitting Materials and Technology, Ministry of Education, Northeast Normal University, Changchun 130024, China*
[g]*MOE Joint Key Laboratory, Institute of Applied Physics and Materials Engineering and Department of Physics and Chemistry, Faculty of Science and Technology, University of Macau, Macao SAR 999078, P. R. China*
[h]*School of Microelectronics, Dalian University of Technology, Dalian, 116024, China*
†Electronic supplementary information (ESI) available. See DOI: https://doi.org/10.1039/d1nr07688d

Unlike twist bilayer graphene, there are two distinct stacking orientations in TMDs semiconductor bilayers, which are R-type stacking (also labeled AA stacking, 0° rotation between two monolayers) and H-type stacking (also labeled AB stacking, 60° or 180° rotation between two monolayers). In homobilayers, H-type bilayer stacking has inversion symmetry, while R-type stacking is broken. As twisting between the layers occurs, three kinds of high-symmetry stacking orders arising from moiré superlattice have been put forward.[13,22] These orders emerge with very different energies and topological natures in near R- and H-type stacking, which means twist-TMDs have an extra degree of freedom for controlling. The stacking orientation, basically, plays a significant role in other vdWs materials as well, for instance, emergent ferroelectric order in parallel stacked bilayer boron nitride (BN)[23–25] and engineering interface polarization based on in-plane inversion symmetry is broken.[26] As of late, interfacial ferroelectricity has been found in R-stacked bilayer TMDs.[27,28] However, it is tricky to predetermine the stacking orientation during the stack-up process, as the absence of distinguishing characteristic edges (especially for metal or chalcogen atoms ended zigzag edge) *via* the exfoliated-edge alignment and second harmonic generation (SHG) methods thus far.

Previous skillful efforts for exfoliating vdWs materials into monolayers mainly focused on crystal quality, size, yield, and scalability. Examples include the solution phase exfoliation,[29] using the cation as the intercalant has scalable and processable advantages at the expense of sizes and quality. Different growth approaches, including chemical vapor deposition (CVD) and molecular beam epitaxy (MBE),[30,31] can produce monolayers on a wafer scale, but polycrystalline and high defect density are still unsurpassed. The original and facile Scotch-tape approach has enabled the highest quality of the monolayers, yet limited by low yield and small size. Recently, utilizing stronger vdWs adhesion between metal and 2D materials to overcome the interlayer vdWs force, high-quality monolayers with large-area, near-unity yields have been produced.[32–35] Unfortunately, all these exfoliation strategies essentially lack sufficient information on the lattice orientation of peeled monolayers. This inadequacy has motivated us to develop innovative peeling approaches with identifiable lattice orientations that simultaneously meet high-quality, large-size, high-yield, which will expedite further advancement in the field of engineering of symmetry breaking, including moiré physics.

After rethinking the process of peeling off, we perceived that disassembling vdWs bulk crystals into monolayers usually overcomes the weaker interlayer attraction in the out-of-plane direction, while in the in-plane it lacks the differentiation along with the specific crystal orientation. For the monolayer, described points group of TMDs of 2H-phase degraded to D_{3h}, with lower symmetry compared to D_{6h} of the bulk. It contains a threefold C_3 rotational symmetry with an S_3 mirror-rotation symmetry, which means there are two typical orientations of armchair (AC) and zigzag (ZZ). Among the ZZ orientation, there are two types of edges: metal-terminated edge and chalcogen-terminated edge. In principle, these three kinds of edges should have very different adsorption energies or bond enthalpy, which will provide the possibility to peel the vdWs crystals from a specific edge.

Here, we demonstrate an edge-locked mechanical exfoliation method for bulk TMDs with discernible orientation, high quality, large-dimension, and high productivity. This method is practical for producing a range of the orientated monolayers vdWs materials, so long as their parent counterparts have the typical atomic edges. Using MoS_2 as a representative system, a pivotal start is illustrated in Fig. 1a; gold (Au) atoms prefer epitaxy along the Mo-terminated ZZ edge, owing to the higher bond strength compared to edges of S-terminated ZZ or AC (details can be seen in the theory section below). Such Au-locking edge will play the role of grasping during the process of peel-off, which induces the monolayer tearing along AC orientation from Mo- to S-terminated of ZZ.

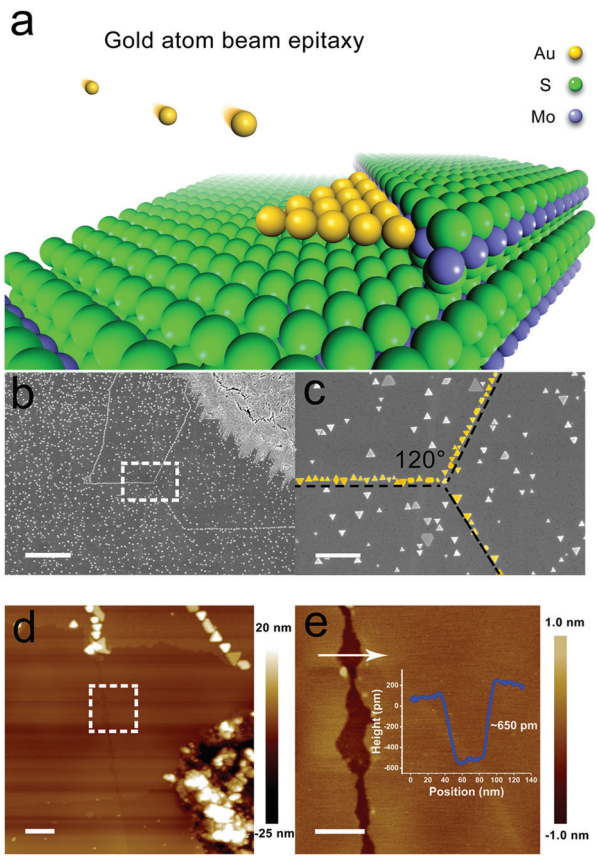

Fig. 1 Gold epitaxy along the atomic steps on the surface of MoS_2 bulk crystals. (a) Schematic illustration of the epitaxial growth of a triangle gold crystal along the zigzag atomic step of MoS_2 bulk crystals by MBE. (b) and (c) False-colour Scanning Electron Microscopy images of the surface of MoS_2 bulk crystals. The yellow triangles (gold nanocrystals) aligned along with one side of the triangles, forming Y-shaped lines with an angle of 120°. Scale bars, (b) 2 μm, (c) 400 nm. (d) and (e) Atomic Force Microscope images were taken near the atomic step of the MoS_2 surface. The height of the step as shown in the blue curve, which is about 650 pm, indicates that it is the monolayer step of MoS_2. Scale bars, (d) 400 nm, (e) 100 nm.

Results

Au-Epitaxy aligns atomic-step edges and theoretical analysis

In order to accurately control the flux of Au atoms reaching the cleaved TMDs surface and to have a sufficient surface relaxation process, we used MBE in this work (Fig. 1a). Owing to the low beam flux and ultrahigh-vacuum conditions (see "Methods"), it can be guaranteed that no extra surface defects will be introduced as in usual evaporation methods (*e.g.* thermal, sputtering). Freshly cleaved bulk TMDs surfaces have flat terraces, which are parted by atomic steps. These atomic steps, essentially, are one-dimensional (1D) defects, serving as a nucleation site, which tend to adsorb or bind heteroatoms to reduce the total energy of the system.[36] Therefore, during the epitaxy of Au crystals, adatoms prefer bonding along these active 1D edges and then crystal growth. The surface morphology, after the initial growth of Au nanocrystallites on the surface of MoS_2 and observed *via* scanning electron microscopy (SEM) and atomic force microscopy (AFM), supports the inference of the nucleation process. As can be seen in Fig. 1b and c, besides the sporadic random distribution on the entire surface, there are also obvious Au nanocrystal grains arranged in a specific direction. In the top view, Au nanocrystal grains appear as equilateral triangular, which means that the crystal orientation is (111). Interestingly, these arranged triangular crystal grains are aligned along the side of each triangle and form an angle of 120° at the point of convergence, which is a consequence of the C_3 symmetry of MoS_2. Such alignment feature indicates that Au atoms nucleate and grow at the ZZ atomic step edges (see the theory part below. They are actually Mo-terminated ZZ edges). In fact, we have examined the morphology of many surfaces after initial epitaxy. We found that only in rare cases, the triangular grains are arranged along the angle bisector of the triangle (ESI Fig. S1†). This means that the Au atoms hardly grow along the AC edges. Atomic steps by arranging Au nanocrystal grains were further analysed by AFM (Fig. 1d and e). The line contour corresponds to the white arrow in Fig. 1e, indicating that the height difference at the steps is 0.65 nm, which equals the thickness of the MoS_2 monolayer. These Au bonded atomic steps are locked during the subsequent peeling process, inducing the oriented peeling.

In order to fully fathom the physical process of the Au atom lateral epitaxy, we carried out first-principles density functional theory (DFT) calculations relating to the initial binding of Au atoms onto the atomic step edges (AC and two kinds ZZ) of MoS_2 and the subsequent alignment between Au nanocrystal grains and atomic edges.

The docking energy (E_d) for Au(111) on the MoS_2 step contains two parts: the surface and the step contact. The surface energy (E_s) only contains the contribution that Au(111) adsorbed on the bottom MoS_2 surface and vdWs energy interaction is in the majority, while the step contact energy (E_c) infers the connection between the S or Mo atom of the MoS_2 step and Au atom of Au(111) closely, which is adjacent to the MoS_2 stage. The step contact energy per length (ε) was defined as E_c/L to describe the ability of docking between MoS_2 and Au(111). L (Å) represents the length of edges, for ZZ steps, L = 22.75 Å, while for AC steps, L = 31.74 Å. Specific formulae for ε, E_s, E_d, and E_c can be found in ESI note 8.† The lower ε (eV Å^{-1}), the greater the ability of docking between MoS_2 and Au(111).

A comparison of the ε values for different step structures of the MoS_2 bilayer is presented in Fig. 2d and ESI Table 1.† Fig. 2a–c shows the top and side views of the DFT-optimized structures of the contact configurations between Au edges and the MoS_2 substrate. The results show that the ε values for the ZZ-Mo direction with A and B steps (ESI Fig. S8a and S8d†) are −1.11 and −0.67 eV Å^{-1}, respectively, while the corresponding values for the AC direction with C and D steps (ESI Fig. S8e and S8f†) are −0.64 and −0.64 eV Å^{-1}, respectively. However, the ε values for the ZZ-S direction with A and B steps (ESI Fig. S8b and S8c†) are −0.19 and −0.07 eV Å^{-1}, respectively. It is clear that the contact in the ZZ direction prefers the A step, while AC presents the same ε of the two steps (ε = −0.64 Å^{-1}). Moreover, the coupling between the ZZ-Mo edge is energetically far greater than that between the ZZ-S edge, which is also similar to the situation described by Yang *et al.*[37] Combing the

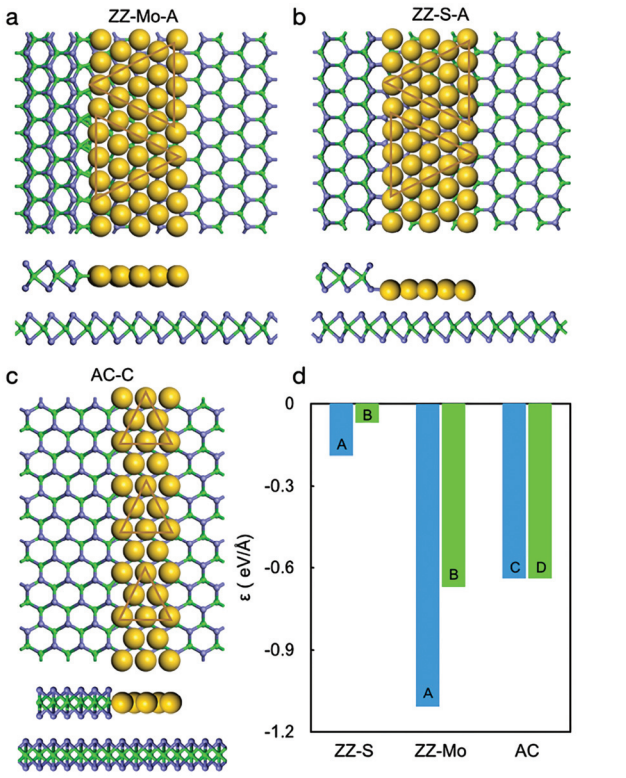

Fig. 2 The ⟨110⟩ direction on the Au(111) surface along two typical MoS_2 step edges and the ⟨112⟩ direction on Au(111) surface along one typical MoS_2 step edge. Atoms in golden, green and blue colors represent the Au, Mo and S atoms, respectively. (a) and (b) Coincide with the zigzag direction (ZZ-Mo and ZZ-S) with A step; (c) armchair (AC) direction with C step. (d) step contact energies per unit of the length of edges between the three edges of the MoS_2 step and Au(111).

optimized structures along the AC direction and the energies above, it seems that the contact is mostly contributed by Mo, and the MoS_2 layer would be stripped from the ZZ-Mo direction. To test the impact of the established model on ε, the model was expanded, *i.e.*, the width was expanded along the AC direction, and it was found that ε has almost no change in value (see ESI Fig. S8†).

From Fig. 2, the MoS_2 step docked by triangular Au(111) presents two scenes: (1) the triangles across the steps, AC edges, *i.e.*, one corner points along the step edge, and one side of the triangles perpendicular to it; (2) One side of a triangle in contact with the step. *i.e.*, one corner contacts the step edge, and one side of the triangle is parallel to it; the ZZ edge. For both the scenes, the arrangement of the directional triangle is ordered and oriented. That is, the orientation of Au(111) on MoS_2 can be used to characterize the edge structure (AC or ZZ) or stack MoS_2 directionally. These scenes present on the step edge have coincided with the submonolayer MoS_2 growth on highly oriented pyrolytic graphite (HOPG)[38] and is in accordance with our SEM and AFM observations shown in Fig. 1 and ESI Fig. S1.† Moreover, a comparison of the ε values for different step structures of Au(111)–WS_2, Au(111)–$MoSe_2$ and Au(111)–WSe_2, as well as Au(111)–MoS_2 is given in ESI Table 1.† The same conclusions are exhibited for MX_2 (M = Mo, W; X = S, Se), that is, the step contact is mostly contributed by Mo or W. This indicates that the MX_2 layers would be stripped from the ZZ-M direction.

Oriented exfoliation and monolayer optical characterization

The schematic diagram of the core procedures of mechanical exfoliation is illustrated in Fig. 3a, where the first procedure is critical, namely, the edge epitaxy of Au atoms in the initial growth stage. A relatively low beam equivalent pressure (BEP), 1.4×10^{-8} Torr, makes the adsorbed Au atoms fully relax, inducing the Mo-terminated ZZ edges to bond uniformly. Uneven bonding edge-induced peeling results can be seen in ESI Fig. S5.† Then, the BEP is slightly increased, and relatively quickly epitaxially forms a continuous Au film. It plays a role in the background vdWs adhesion in the out-of-plane direction and protects the stripped layers from contamination, during the subsequent peeling process. The thermal release tape is gently pressed on top of the Au film to form an even and close contact. The top layer of TMDs is peeled off from one side and the monolayer is exfoliated along the tearing AC edges under the combined action of the adhesion forces from two directions, *viz.*, out-of-plane (from the topmost Au film) and in-plane (from the Au bonded ZZ edges). After that, it was transferred onto the target substrate, and the thermal release tape was removed by heating it to the right temperature. A mild iodine/potassium iodide (I_2/KI) solution was applied to etch away the Au film and dissolve possible residues of the thermal release tape with acetone. Finally, monolayer and multilayer TMDs were obtained. Among these different thickness layers, a large-area monolayer has straight AC edges. Its lateral dimensions reach the sub-millimeter scales (Fig. 3c), which are

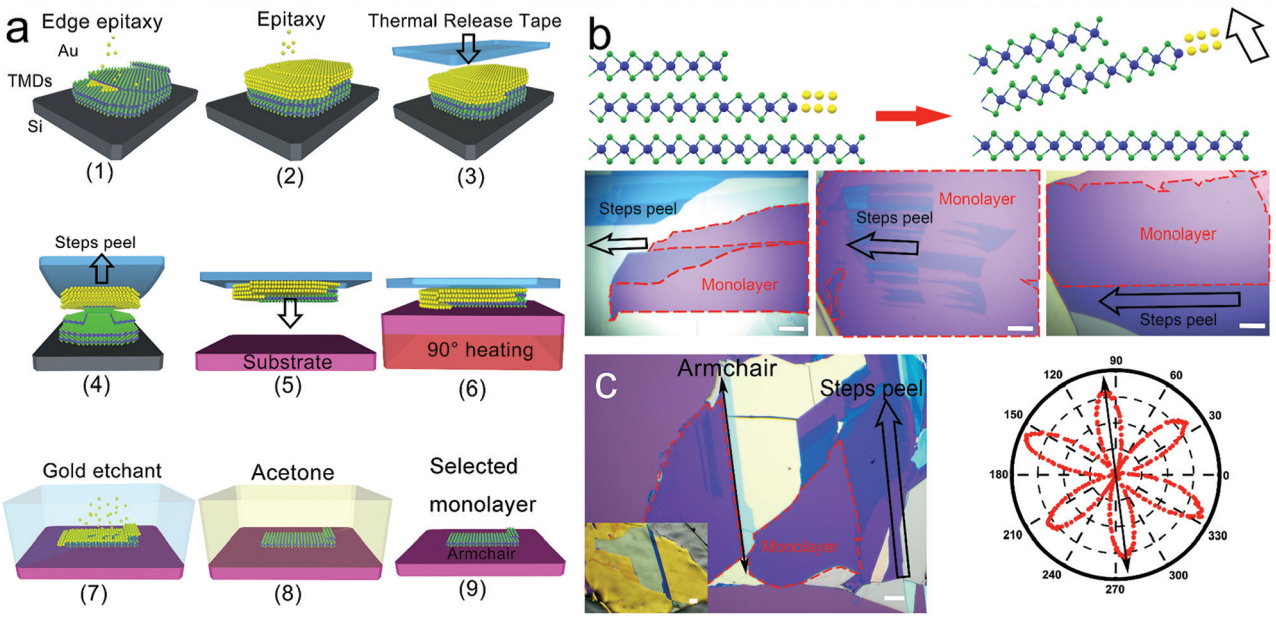

Fig. 3 Methods of mechanical exfoliation along the armchair direction. (a) Schematic illustration: (1) Slowly epitaxy growth of gold on MoS_2 bulk crystals on silicon by MBE; (2) Epitaxy gold until gold atoms cover the surface; (3) Sticking thermal release tape to the surface of the gold film; (4) Pulling up thermal release tape and MoS_2 bulk crystals peeling off along the steps of the zigzag direction; (5) Sticking thermal release tape, gold and MoS_2 to the surface of the substrate; (6) 90° heating; (7) Etching gold by KI/I_2 solutions; (8) Cleaning residues by acetone; (9) Obtaining MoS_2 monolayers on the surface of SiO_2, which have a long armchair edge. (b) Schematic illustration and optical images of mechanical exfoliation from zigzag-Mo to zigzag-S directions. Scale bar, 10 μm. (c) Optical images of large areas and along the armchair direction of monolayer MoS_2 crystals. Scale bars, 50 μm.

limited mainly by the sizes of the terraces separated by atomic steps. The peeled surface layers (the inset of Fig. 3c) can be completely transferred to the substrate using this method. Since the second-order susceptibility tensor $\chi^{(2)}$ for the non-centrosymmetric monolayer TMDs along the AC direction is non-vanishing, the linear polarization-dependent SHG can identify the orientation and symmetry.[39] As shown in Fig. 3c, the polar diagram of the SHG intensity represents the AC orientation in parallel with torn edges, useful for precise alignment between each layer in homo- and hetero-stacking. Substantially, equal polarization SHG intensity distribution also illustrates that the strain that can cause the lattice vector change is insignificant after this peeling-transfer process. Notably, along the peeling direction, the number of layers generally presents the characteristics of the transition from the monolayer to bilayer and even multilayer, which is the consequence of the 2H stacking order (the atomic edges of the adjacent terraces have different termination atoms), as shown in Fig. 3b. This also served as orientation recognition for the following artificial stacking. The resulting optical images and SHG intensity polar diagrams of the achieved monolayers of WS_2, $MoSe_2$, and WSe_2 are shown in ESI Fig. S2,† which exhibit the same results.

Photoluminescence (PL) and Raman spectroscopy were used to evaluate the crystal quality of TMDs monolayers. As shown in Fig. 4a, there are two distinct emission peaks at room temperature, located at 1.86 eV and 2.02 eV, which correspond to A- and B-exciton, respectively, for a monolayer MoS_2 on Si/SiO_2 (285 nm) substrate. Two typical Raman vibrational modes are observed in Fig. 4b, in which, the spacing between E^1_{2g} and A_{1g} was 19.8 cm^{-1} (determined by the interlayer interactions), supporting one layer thickness. PL and Raman 2D imaging of the monolayer MoS_2 are shown in ESI Fig. S4,† in which, a spatial homogeneous result of the PL peak and phonon wavenumber spacing are displayed. The results for WS_2, $MoSe_2$, and WSe_2 are shown in ESI Fig. S3,† confirming that the monolayers are of high quality.

Artificial stacking and energy band tuning

These stripped monolayers provide the prerequisite for the stacking orientation known in advance. Based on the judgment of orientation, mentioned above, two types of bilayer stacking ordering (H-type and R-type) are intentionally constructed, as shown in Fig. 5. The detailed stacking process is shown in ESI Fig. S7,† in which the upper monolayers are transferred on transparent polydimethylsiloxane (PDMS) directly for a stamp dry transfer method. H-type stacking homobilayer MoS_2 exhibits inversion symmetry, resulting in a weaker SHG intensity compared to the monolayer region, as shown in Fig. 5a. Meanwhile, R-type stacking has the opposite situation, inversion symmetry breaking homobilayer has stronger SHG intensity, due to interference coherent enhanced from the individual monolayers (Fig. 5b). Pre-identification of crystal orientation improves the efficiency of symmetry control in this study.

Furthermore, straight and longer armchair edges, obtained by our method, provide a more accurate alignment basis for twisted stacking. As illustrated in the inset of Fig. 6, a twisted

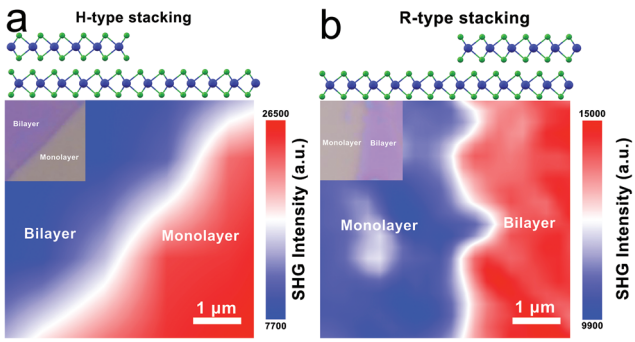

Fig. 5 SHG mapping of H-type (anti-parallel) and R-type (parallel) stacking MoS_2 crystals. (a) Intensity of the anti-parallel bilayer MoS_2 crystals is weaker than that of the monolayer. (b) The intensity of parallel bilayer MoS_2 crystals is stronger than the monolayer. Scale bars, 1 μm.

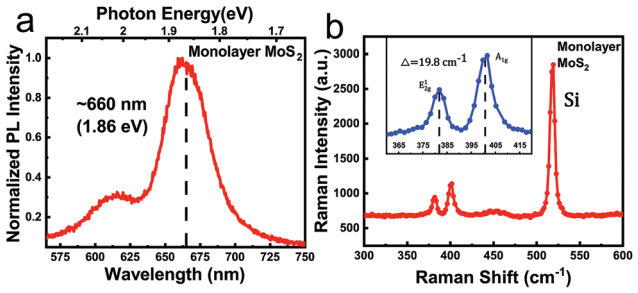

Fig. 4 PL and Raman spectra of monolayer MoS_2 at room temperature with the excitation laser wavelength of 532.18 nm. (a) Normalized PL spectra intensity of monolayer MoS_2. (b) Raman shift of in-plane E^1_{2g} mode and out-of-plane A_{1g} mode of monolayer MoS_2.

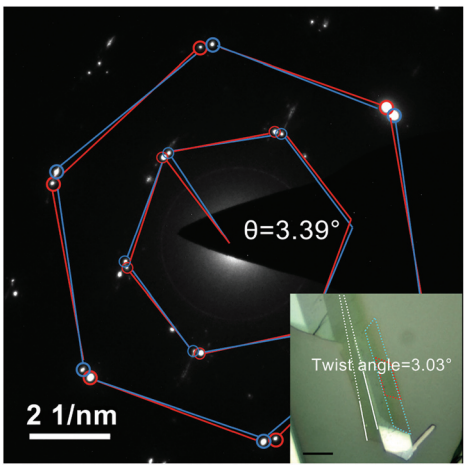

Fig. 6 Selected area electron diffraction (SAED) image of twist bilayer MoS_2/MoS_2. The twist angle is 3.39° in the SAED image of the bilayer MoS_2/MoS_2. The twist angle is 3.03° from measuring the angle between two straight edges in optical images of the twist bilayer MoS_2/MoS_2 in the insert figure (scale bar, 10 μm).

bilayer MoS_2 with a designed angle of 3.03° is fabricated by angular rotating between two AC edges. The actual twist-angle, 3.39° (Fig. 6), is confirmed by selected area electron diffraction (SAED), which is close to the designed rotation angle, indicating the accuracy of using a longer AC edge. Additionally, surrounding each pair of hexagonal diffraction spots, high order satellite spots have been observed, which are caused by interlayer interaction and atomic reconstruction of thebtwisted-bilayer.

The large-size high-quality stacked bilayer allows us to obtain the electronic structure with standard angle-resolved photoemission spectroscopy (ARPES) technique using a conventional setup with a hemispherical electron energy analyzer without microscopic capabilities. Fig. 7 presents M–Γ–K slices, showing the important features within 4 eV under the Fermi level for the H-type (Fig. 7a, c and e) and R-type (Fig. 7b, d and f) stacked MoS_2 bilayers. All features of the valence bands are well resolved, implying that the method we developed could well keep the sample surface from deterioration and contamination. The band structure over the entire surface-Brillouin zone reveals that the valence band maximum (VBM) at Γ is indeed the highest occupied state for both the H-type and R-type stacked bilayers, affirming the indirect nature of the bilayer MoS_2 bandgap. Note that our ARPES data clearly show an energy difference between the valence band maximum at Γ and K for H- and R-stacked bilayers, as shown in Fig. 7a and b, and their corresponding second-derivative spectra Fig. 7c and d. The energy difference is further determined in the corresponding energy distribution curves (EDCs), as shown in Fig. 7e and f. We know that the VBM at Γ is derived from the out-of-plane S p_z and Mo d_{z^2} orbitals, while the VBM at K is mostly derived from Mo $d_{x^2-y^2/xy}$ orbitals.[40] Thus, the energy of the valence band maxima at Γ is sensitive to the out-of-plane interlayer coupling, as compared to the K point. In this study, according to previous reports,[41,42] the R-stacked bilayer has a smaller interlayer spacing compared to the H-stacked one, which induces stronger interlayer coupling between the out-of-plane orbitals in R-type stacking order, and gives rise to a upshift in the energy of the Γ point, as observed in Fig. 7.

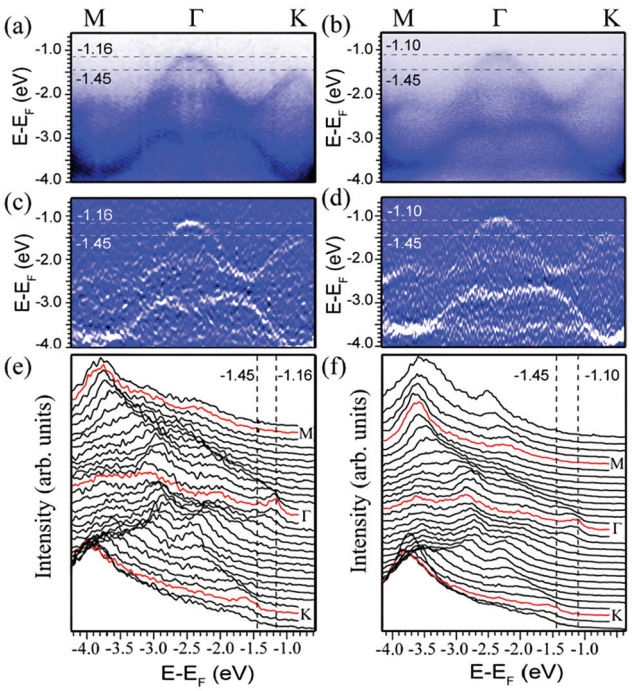

Fig. 7 ARPES measurement of the sub-millimeter scale stacked bilayer MoS_2. (a) and (b) The band structure along the M–Γ–K high symmetry direction for H-type and R-type stacked MoS_2 bilayer. (c) and (d) Second-derivative spectra of (a) and (b), respectively. (e) and (f) The corresponding energy distribution curves (EDCs) along the high symmetry direction. The dashed lines indicate the energy difference between valence band maximum (VBM) at Γ and K for the H-type and R-type stacked MoS_2 bilayer.

In summary, we have developed an orientation recognizable mechanical exfoliation method for the disassembly of 2D vdWs materials. The obtained monolayers have high-quality, large-dimension, and are torn along the armchair orientation, which is verified by PL, Raman, and SHG. As the orientation information is known in advance, the artificial stacking orderings (R-type and H-type) with different symmetries and band structures have been successfully realized without accidents, which was demonstrated by SHG mapping and ARPES. This strategy is not only effective for MoS_2, WS_2, $MoSe_2$, WSe_2, as confirmed from experiments, but is also promising for other TMDs, such as Nb-, Ta-, or Ti-based TMDs, which, as long as choosing the appropriate metals, meet the requirements of lateral epitaxy and damage-free etching. The clear-cut orientation of monolayers will make the research for twistronics, including moiré physics or band topology in vdWs stacking, more facilitated.

Methods

Gold atoms epitaxy on the surface of transition metal dichalcogenides (TMDs) bulk crystals

Freshly cleaved TMDs bulk crystals (6 Carbon Technology, Shenzhen) were transferred to the cleaned silicon (Si) wafer surface by using thermal release tape (TRT) with a releasing temperature of 90 °C. Before the gold (Au) atom epitaxy in the main chamber of the molecular beam epitaxy (MBE) system (P600, DCA Instruments, Finland), samples were transported to an ultrahigh vacuum (UHV) subsystem (base pressure of 3×10^{-9} Torr), vacuum interconnected with the main chamber, for the surface cleaning under the condition of heating at 350 °C for 12 hours. During the epitaxy, the K-cell containing Au (6 N grade) was maintained at 1260 °C to form a steady Au atom beam equivalent pressure (BEP), which was 1.4×10^{-8} Torr, while the TMDs/Si substrate was maintained at 200 °C. The temperature of the K-cell was increased to 1280 °C for afterward Au film growth.

Mechanical exfoliation

Firstly, TRT (releasing temperature 90 °C) was gently pressed onto the surface of the prepared Au/TMDs/Si following a

peeling-off process. Under the action of the combination of adhesion from two directions, the topmost layers of bulk TMDs including oriented monolayers were stripped, which were attached to the Au surface. The TRT/Au/TMDs were subsequently transferred onto the desired substrate. Secondly, the TRT was removed by heating at 90 °C. The Au film was dissolved in a solution containing potassium iodide (KI) and iodide (I_2) (35 g KI and 13 g I_2 dissolved in 100 ml deionized water). Finally, the monolayer of TMDs was further rinsed with deionized water and acetone for 5 minutes and dried using the N_2 flow.

Morphological and crystal structure characterization

The surface topography of bulk MoS_2, at the initial stage of Au epitaxy, was measured using an atomic force microscope (Multimode8, Bruck Instruments, Germany) and a scanning electron microscope (S-4800, Hitachi Instruments, Japan). The selected area electron diffraction (SAED) of the MoS_2 bilayer was measured using the Field Emission Transmission Electron Microscope (TEM) (Tecnai G2 F20, FEI, American) with 200 kV accelerating voltage.

Optical characterization

The optical images were obtained using a custom-built microscopy system using a 20× objective lens. Photoluminescence (PL), Raman spectra and the polarization-dependent second harmonic generation (SHG) were performed at room temperature on a laser scanning system (ScanPro Advance, Metatest, China). The laser-focused spot was about 1 μm diameter using a 100× objective lens (Olympus Corporation, Japan). The wavelength of the excitation source for PL and Raman was 532.18 nm with a power of 0.1 mW. Polarization-dependent SHG was performed using a 1064 nm picosecond laser (10 ps), with two polarizers (polarizer and analyzer) equipped with a rotating half-wave plat between them.

SAED sample preparation

Mechanically exfoliated MoS_2 monolayers were firstly prepared onto polydimethylsiloxane (PDMS). 50 μL polycarbonate (PC) solution (8% weight in trichloromethane) was dropped on a glass slide and self-leveling a PC film. Two of the MoS_2 monolayers were stacked from PDMS to the PC film by heating to 80 °C for 10 minutes. The twisted angle was about 3.03° by aligning the straight torn edges. Then, the PC film was peeled from the glass slide and placed onto PDMS, forming a stamp of twist-bilayer MoS_2/PC/PDMS. Finally, the twist-bilayer MoS_2 was transferred onto a carbon-supported copper grid by heating to 180 °C for 2 minutes. The PC was removed using trichloromethane and acetone.

SHG sample preparation

Two groups of mechanical exfoliation MoS_2 monolayers were firstly prepared onto PDMS and Si/SiO_2 (285 nm). Then, they were aligned-stacked from PDMS to Si/SiO_2 (285 nm) with a rotation angle close to 0° or 180° by heating to 80 °C for 10 minutes. Stacking ordering was predetermined, as shown in ESI Fig. S7.†

Angle-resolved photoemission spectroscopy measurement

High-resolution ARPES measurements were performed with incident photon energies of 140 eV at beamline 03U of the Shanghai synchrotron radiation facility (SSRF). The ARPES system was equipped with a Scienta-Omicron DA30 electron energy analyzer. During measurements, the vacuum was better than 8.0×10^{-11} Torr and the temperature was kept at around 15 K. Energy resolutions were better than 20 meV. The beam size of the synchrotron radiation is roughly under 100 micrometers. For ARPES measurements, the samples were transferred onto an Au/MgO substrate. An annealing process lower than 300 °C for 12 h was performed to clean the surfaces after loading them into a high vacuum chamber.

Density functional theory (DFT) calculations

Calculation methods. DFT calculations were performed by the plane-wave method as implemented in the Vienna Ab Initio Simulation Package (VASP).[43,44] The electron exchange–correlation and the ion-electron interactions were treated by Perdew–Burke–Ernzerhof functionals (PBE)[45] and projector-augmented wave (PAW)[46] potentials, and van der Waals (vdW) corrections were considered by the zero damping DFT-D3 method.[47,48] An energy cutoff of 400 eV for the plane waves was employed, and the convergence criteria energy and force were set to 10^{-4} eV and 0.1 eV $Å^{-1}$, respectively, for structural relaxation. Only the Gamma point was used due to the large supercell. The periodic lattice perpendicular to the plane direction was larger than 20 Å to avoid artificial interactions.

Model establishment. The optimized lattice constant of Au and MoS_2 are 4.16 and 3.18 Å, respectively, which is in good agreement with the experimental values of 4.072 and 3.169 Å.[49,50] The Au(111)–MoS_2 overlayer was modeled by an $\left(8 \times 6\sqrt{3}\right)$ Au(111) on $\left(7 \times 6\sqrt{3}\right)$ MoS_2 bilayer to simulate the contact configurations between Au edges and the MoS_2 substrate with a lattice mismatch of ~5.6%. The MoS_2 bilayer with 168 molybdenum (Mo), 336 sulfur (S) atoms and the top Au monolayer with 96 atoms as the initial structure (lattice parameters a = 22.85 Å, b = 31.74 Å). Then, the overlayer was cut and docked to two kinds of step edges: armchair (AC) direction and zigzag direction (ZZ-Mo and ZZ-S). 2 (named A step) or 3 (named B step) rows of MoS_2 along the ZZ direction and 3 (named C step) or 2.5 (named D step) rows along the AC direction were remaining to simulate the step structure of MoS_2, followed by placing the remaining 5 and 3 rows Au of Au(111) after cutting onto the ZZ and AC edges with geometric relaxation, respectively. The stage was wide enough to reduce the fluctuation of step atoms on the MoS_2 surface. The ZZ edge of MoS_2 was parallel to the ⟨110⟩ direction of Au(111) and the AC edge of MoS_2 was parallel to the ⟨112⟩ direction of Au(111). The geometries are presented in Fig. 2 and ESI Fig. S8.† Moreover, we performed additional test calculations to further verify the reliability of the calculation model (ESI Fig. S8†).

Author contributions

Y. S.: methodology, resources, investigation, visualization, formal analysis, writing-original draft. X. H.: conceptualization, resources, funding acquisition, formal analysis, writing-original draft, writing-review and editing, visualization, project administration. B. L.: resources, methodology. X.L.: formal analysis, formal analysis, writing-original draft. Y. C.: resources, investigation. J. S.: resources, investigation, formal analysis, visualization, writing-original draft. J. Y.: resources, investigation. Y.: resources, investigation. Y.Z.: resources, investigation. W. Z.: resources, investigation. S. W.: resources, investigation. W.: resources, investigation. H.: resources, investigation. Z. Z.: resources, investigation. D. W.: resources, investigation. D.Z.: funding acquisition. In detail, X.H. conceived the project. X.H. and D. Z. supervised this work. X. H., Y. S. and B. H. designed the experiments. X. L. performed the DFT calculations. Y. S. and H. prepared the mechanical exfoliation samples. Y. S., J. Y., Y., and Y. Z. performed the Raman, PL and SHG measurements. X. H. and B. H. performed the gold growth by MBE. Y. S. and W. performed the AFM measurements. J. S. and Y. C. performed the ARPES measurement. X. H., Y. S., and H. prepared the stacking samples. B. H., Y. S., H., and Z. Z. performed the SEM and SAED measurements. X. H., Y. S., X. L., and J. S. wrote the manuscript with inputs from all authors. All authors discussed the results and commented on the paper.

Conflicts of interest

The authors declare no competing interests.

Acknowledgements

This research is mainly supported by the National Natural Science Foundation of China (Grant No. 11727902 and 62074146). S. P. and X. H. gratefully acknowledge support from Multi-Year Research Grants (MYRG2020-00207-IAPME) from Research and Development Office at University of Macau. X. L. acknowledges generous financial support by the National Natural Science Foundation of China (Grant No. 21903036). Y. Z. acknowledges support from Program of National Natural Science Foundation of China (Grant No. 12004069). W. Z. acknowledges support from the Program of National Natural Science Foundation of China (Grant No. 12074060 and 11874104), the Fund from Jilin Province (No. YDZJ202101ZYTS133 and JJKH20211273KJ) and the Fundamental Research Funds for the Central Universities (No. 2412019BJ006 and 2412021ZD012). J. S. and D. W. acknowledge the fund support from National Natural Science Foundation of China (U2032208). Part of this research also used beam line 02B of the Shanghai Synchrotron Radiation Facility, which is supported by the ME2 project under Contract No. 11227902 from the National Natural Science Foundation of China.

Notes and references

1 R. Bistritzer and A. H. MacDonald, *Proc. Natl. Acad. Sci. U. S. A.*, 2011, **108**, 12233–12237.
2 C. Zhang, C.-P. Chuu, X. Ren, M.-Y. Li, L.-J. Li, C. Jin, M.-Y. Chou and C.-K. Shih, *Sci. Adv.*, 2017, **3**, e1601459.
3 Y. Cao, V. Fatemi, S. Fang, K. Watanabe, T. Taniguchi, E. Kaxiras and P. Jarillo-Herrero, *Nature*, 2018, **556**, 43–50.
4 Y. Cao, V. Fatemi, A. Demir, S. Fang, S. L. Tomarken, J. Y. Luo, J. D. Sanchez-Yamagishi, K. Watanabe, T. Taniguchi, E. Kaxiras, R. C. Ashoori and P. Jarillo-Herrero, *Nature*, 2018, **556**, 80–84.
5 C. L. Tschirhart, M. Serlin, H. Polshyn, A. Shragai, Z. Xia, J. Zhu, Y. Zhang, K. Watanabe, T. Taniguchi, M. E. Huber and A. F. Young, *Science*, 2021, **372**, 1323–1327.
6 F. C. Wu, T. Lovorn, E. Tutuc and A. H. MacDonald, *Phys. Rev. Lett.*, 2018, **121**, 026402.
7 H. Pan, F. Wu and S. D. Sarma, *Phys. Rev. Res.*, 2020, **2**, 033087.
8 Y. H. Tang, L. Z. Li, T. X. Li, Y. Xu, S. Liu, K. Barmak, K. Watanabe, T. Taniguchi, A. H. MacDonald, J. Shan and K. F. Mak, *Nature*, 2020, **579**, 353–358.
9 E. C. Regan, D. Q. Wang, C. H. Jin, M. I. Utama, B. N. Gao, X. Wei, S. H. Zhao, W. Y. Zhao, Z. C. Zhang, K. Yumigeta, M. Blei, J. D. Carlstrom, K. Watanabe, T. Taniguchi, S. Tongay, M. Crommie, A. Zettl and F. Wang, *Nature*, 2020, **579**, 359–363.
10 B. Padhi, R. Chitra and P. W. Phillips, *Phys. Rev. B: Condens. Matter Mater. Phys.*, 2021, **103**, 125146.
11 Y. Zhou, J. Sung, E. Brutschea, I. Esterlis, Y. Wang, G. Scuri, R. J. Gelly, H. Heo, T. Taniguchi, K. Watanabe, G. Zarand, M. D. Lukin, P. Kim, E. Demler and H. Park, *Nature*, 2021, **595**, 48–52.
12 E. Y. Andrei, D. K. Efetov, P. Jarillo-Herrero, A. H. MacDonald, K. F. Mak, T. Senthil, E. Tutuc, A. Yazdani and A. F. Young, *Nat. Rev. Mater.*, 2021, **6**, 201–206.
13 S. Shabani, D. Halbertal, W. Wu, M. Chen, S. Liu, J. Hone, W. Yao, D. N. Basov, X. Zhu and A. N. Pasupathy, *Nat. Phys.*, 2021, **17**, 720–725.
14 C. Anton-Solanas, M. Waldherr, M. Klaas, H. Suchomel, T. H. Harder, H. Cai, E. Sedov, S. Klembt, A. V. Kavokin, S. Tongay, K. Watanabe, T. Taniguchi, S. Hofling and C. Schneider, *Nat. Mater.*, 2021, **20**, 1233–1239.
15 L. Zhang, F. C. Wu, S. C. Hou, Z. Zhang, Y. H. Chou, K. Watanabe, T. Taniguchi, S. R. Forrest and H. Deng, *Nature*, 2021, **591**, 61–65.
16 X. Huang, T. M. Wang, S. N. Miao, C. Wang, Z. P. Li, Z. Lian, T. Taniguchi, K. Watanabe, S. Okamoto, D. Xiao, S. F. Shi and Y. T. Cui, *Nat. Phys.*, 2021, **17**, 715–719.
17 C. H. Jin, Z. Tao, T. X. Li, Y. Xu, Y. H. Tang, J. C. Zhu, S. Liu, K. Watanabe, T. Taniguchi, J. C. Hone, L. Fu, J. Shan and K. F. Mak, *Nat. Mater.*, 2021, **20**, 940–944.
18 D. M. Kennes, M. Claassen, L. D. Xian, A. Georges, A. J. Millis, J. Hone, C. R. Dean, D. N. Basov, A. N. Pasupathy and A. Rubio, *Nat. Phys.*, 2021, **17**, 155–163.

19 L. Wang, E. M. Shih, A. Ghiotto, L. Xian, D. A. Rhodes, C. Tan, M. Claassen, D. M. Kennes, Y. S. Bai, B. Kim, K. Watanabe, T. Taniguchi, X. Y. Zhu, J. Hone, A. Rubio, A. N. Pasupathy and C. R. Dean, *Nat. Mater.*, 2020, **19**, 861–866.
20 F. C. Wu, T. Lovorn, E. Tutuc, I. Martin and A. H. MacDonald, *Phys. Rev. Lett.*, 2019, **122**, 086402.
21 Y. Xu, S. Liu, D. A. Rhodes, K. Watanabe, T. Taniguchi, J. Hone, V. Elser, K. F. Mak and J. Shan, *Nature*, 2020, **587**, 214–218.
22 Z. M. Zhang, Y. M. Wang, K. Watanabe, T. Taniguchi, K. Ueno, E. Tutuc and B. J. LeRoy, *Nat. Phys.*, 2020, **16**, 1093–1096.
23 M. V. Stern, Y. Waschitz, W. Cao, I. Nevo, K. Watanabe, T. Taniguchi, E. Sela, M. Urbakh, O. Hod and M. Ben Shalom, *Science*, 2021, **372**, 1462–1466.
24 K. Yasuda, X. R. Wang, K. Watanabe, T. Taniguchi and P. Jarillo-Herrero, *Science*, 2021, **372**, 1458–1462.
25 C. R. Woods, P. Ares, H. Nevison-Andrews, M. J. Holwill, R. Fabregas, F. Guinea, A. K. Geim, K. S. Novoselov, N. R. Walet and L. Fumagalli, *Nat. Commun.*, 2021, **12**, 347.
26 T. Akamatsu, T. Ideue, L. Zhou, Y. Dong, S. Kitamura, M. Yoshii, D. Y. Yang, M. Onga, Y. Nakagawa, K. Watanabe, T. Taniguchi, J. Laurienzo, J. W. Huang, Z. L. Ye, T. Morimoto, H. T. Yuan and Y. Iwasa, *Science*, 2021, **372**, 68–72.
27 X. Wang, K. Yasuda, Y. Zhang, S. Liu, K. Watanabe, T. Taniguchi, J. Hone, L. Fu and P. Jarillo-Herrero, *arXiv preprint*, 2021, Preprint at **https://arxiv.org/abs/2108.07659**.
28 A. Weston, E. G. Castanon, V. Enaldiev, F. Ferreira, S. Bhattacharjee, S. Xu, H. Corte-Leon, Z. Wu, N. Clark and A. Summerfield, *arXiv preprint*, 2021, Preprint at **https://arxiv.org/abs/2108.06489**.
29 J. H. Han, M. Kwak, Y. Kim and J. Cheon, *Chem. Rev.*, 2018, **118**, 6151–6188.
30 Z. Y. Cai, B. L. Liu, X. L. Zou and H. M. Cheng, *Chem. Rev.*, 2018, **118**, 6091–6133.
31 D. Y. Fu, X. X. Zhao, Y. Y. Zhang, L. J. Li, H. Xu, A. R. Jang, S. I. Yoon, P. Song, S. M. Poh, T. H. Ren, Z. Ding, W. Fu, T. J. Shin, H. S. Shin, S. T. Pantelides, W. Zhou and K. P. Loh, *J. Am. Chem. Soc.*, 2017, **139**, 9392–9400.
32 F. Liu, W. J. Wu, Y. S. Bai, S. H. Chae, Q. Y. Li, J. Wang, J. Hone and X. Y. Zhu, *Science*, 2020, **367**, 903–906.
33 Y. Huang, Y. H. Pan, R. Yang, L. H. Bao, L. Meng, H. L. Luo, Y. Q. Cai, G. D. Liu, W. J. Zhao, Z. Zhou, L. M. Wu, Z. L. Zhu, M. Huang, L. W. Liu, L. Liu, P. Cheng, K. H. Wu, S. B. Tian, C. Z. Gu, Y. G. Shi, Y. F. Guo, Z. G. Cheng, J. P. Hu, L. Zhao, G. H. Yang, E. Sutter, P. Sutter, Y. L. Wang, W. Ji, X. J. Zhou and H. J. Gao, *Nat. Commun.*, 2020, **11**, 2453.
34 J.-Y. Moon, M. Kim, S.-I. Kim, S. Xu, J.-H. Choi, D. Whang, K. Watanabe, T. Taniguchi, D. S. Park, J. Seo, S. H. Cho, S.-K. Son and J.-H. Lee, *Sci. Adv.*, 2020, **6**, eabc6601.
35 A. Quellmalz, X. J. Wang, S. Sawallich, B. Uzlu, M. Otto, S. Wagner, Z. X. Wang, M. Prechtl, O. Hartwig, S. W. Luo, G. S. Duesberg, M. C. Lemme, K. B. Gylfason, N. Roxhed, G. Stemme and F. Niklaus, *Nat. Commun.*, 2021, **12**, 917.
36 Z. Y. Zhang, Y. R. Ying, M. Xu, C. L. Zhang, Z. G. Rao, S. M. Ke, Y. B. Zhou, H. T. Huang and L. F. Fei, *Nano Lett.*, 2020, **20**, 8112–8119.
37 P. F. Yang, S. Q. Zhang, S. Y. Pan, B. Tang, Y. Liang, X. X. Zhao, Z. P. Zhang, J. P. Shi, Y. H. Huan, Y. P. Shi, S. J. Pennycook, Z. F. Ren, G. H. Zhang, Q. Chen, X. L. Zou, Z. F. Liu and Y. F. Zhang, *ACS Nano*, 2020, **14**, 5036–5045.
38 C. I. Lu, C. J. Butler, J. K. Huang, C. R. Hsing, H. H. Yang, Y. H. Chu, C. H. Luo, Y. C. Sun, S. H. Hsu, K. H. O. Yang, C. M. Wei, L. J. Li and M. T. Lin, *Appl. Phys. Lett.*, 2015, **106**, 181904.
39 W. T. Hsu, Z. A. Zhao, L. J. Li, C. H. Chen, M. H. Chiu, P. S. Chang, Y. C. Chou and W. H. Chang, *ACS Nano*, 2014, **8**, 2951–2958.
40 G. B. Liu, W. Y. Shan, Y. G. Yao, W. Yao and D. Xiao, *Phys. Rev. B: Condens. Matter Mater. Phys.*, 2013, **88**, 085433.
41 P. C. Yeh, W. Jin, N. Zaki, J. Kunstmann, D. Chenet, G. Arefe, J. T. Sadowski, J. I. Dadap, P. Sutter, J. Hone and R. M. Osgood, *Nano Lett.*, 2016, **16**, 953–959.
42 J. Kunstmann, F. Mooshammer, P. Nagler, A. Chaves, F. Stein, N. Paradiso, G. Plechinger, C. Strunk, C. Schuller, G. Seifert, D. R. Reichman and T. Korn, *Nat. Phys.*, 2018, **14**, 801–805.
43 G. Kresse and J. Furthmuller, *Comput. Mater. Sci.*, 1996, **6**, 15–50.
44 G. Kresse and J. Furthmuller, *Phys. Rev. B: Condens. Matter Mater. Phys.*, 1996, **54**, 11169–11186.
45 J. P. Perdew, K. Burke and M. Ernzerhof, *Phys. Rev. Lett.*, 1996, **77**, 3865–3868.
46 P. E. Blochl, *Phys. Rev. B: Condens. Matter Mater. Phys.*, 1994, **50**, 17953–17979.
47 S. Grimme, J. Antony, S. Ehrlich and H. Krieg, *J. Chem. Phys.*, 2010, **132**, 154104.
48 S. Grimme, S. Ehrlich and L. Goerigk, *J. Comput. Chem.*, 2011, **32**, 1456–1465.
49 I. K. Suh, H. Ohta and Y. Waseda, *J. Mater. Sci.*, 1988, **23**, 757–760.
50 V. Petkov, S. J. L. Billinge, P. Larson, S. D. Mahanti, T. Vogt, K. K. Rangan and M. G. Kanatzidis, *Phys. Rev. B: Condens. Matter Mater. Phys.*, 2002, **65**, 092105.